RESEARCH ARTICLE

Ion-sieving MXene flakes with quantum dots enable high plating capacity for dendrite-free Zn anodes

Xinlong Liu | Bingang Xu ⓘ | Shenzhen Deng | Jing Han | Yongling An | Jingxin Zhao | Qingjun Yang | Yana Xiao | Cuiqin Fang

Nanotechnology Center, School of Fashion and Textiles, The Hong Kong Polytechnic University, Kowloon, Hong Kong, China

Correspondence
Bingang Xu, Nanotechnology Center, School of Fashion and Texitles, The Hong Kong Polytechnic University, Kowloon, 999077, Hong Kong, China.
Email: tcxubg@polyu.edu.hk

Abstract

The commercial utilization of Zn metal anodes with high plating capacity is significantly hindered by the uncontrolled growth of dendrites and associated side reactions. Herein, a robust artificial ion-sieving MXene flake (MXF)-coating layer, with abundant polar terminated groups, is constructed to regulate the interfacial Zn^{2+} deposition behavior. In particular, the fragmented MXF coupled with in situ generated quantum dots not only has strong Zn affinity to homogenize electric fields but also generates numerous zincophilic sites to reduce nucleation energy, thus securing a uniform dendrite-free surface. Additionally, the porous coating layer with polar groups allows the downward diffusion of Zn^{2+} to achieve bottom-up deposition and repels the excessive free water and anions to prevent parasitic reactions. The ion-sieving effect of MXF is firmly verified in symmetric cells with high areal capacity of 10–40 mAh cm^{-2} (1.0 mA cm^{-2}) and depth of discharge of 15%–60%. Therefore, the functional MXF-coated anode manifests long-term cycling with 2700 h of stable plating/stripping in Zn‖Zn cell. Such rational design of MXF protective layer breaks new ground in developing high plating capacity zinc anodes for practical applications.

KEYWORDS
high plating capacity, ion sieving, MXene, protective layer, zinc anode

1 | INTRODUCTION

Zinc-ion batteries (ZIBs) are rapidly emerging as compelling choices for next-generation energy storage devices owing to their advantages of intrinsic safety, high capacity of metallic Zn, affordability, and adequate natural reserves.[1–4] Catalyzed by the burgeoning demand in the wearable technology market, ZIBs have seen substantial progress in the realms of cathode material and electrolyte configuration. However, several pressing issues associated with the Zn electrode considerably hinder the practical applications of ZIBs. Notably, the uncontrolled growth of dendrites is detrimental, which can cause short circuits in the batteries and thus reduce the cycling lifespan.[5,6] Furthermore, the accumulation of by-products (e.g., H_2 and $ZnSO_4(OH)_6 \cdot xH_2O$ [ZHS]), resulting from hydrogen evolution reaction (HER) and corrosion, severely compromises the Coulombic efficiency (CE), and, if unaddressed,

ultimately leads to battery failure. These obstacles necessitate innovative solutions to advance ZIB technology.

Several strategies have been proposed to enhance the electrochemical performances of zinc anodes. For example, the regulation of electrolytes with different additives and solvents can modulate the solvation structure and stabilize the interfacial reaction from Zn^{2+} to Zn^0.[7,8] Nonetheless, it is unsuitable for practical applications due to the high cost of highly concentrated electrolytes and the continuous consumption of additives. Additionally, alloying anode is another alternative strategy with the ability to alter the composition and electronic properties of anodes, leading to improved plating/stripping stability and reduced reactivity, which can optimize the surface activity, improve charge transfer kinetics, and mitigate side reactions at the electrode–electrolyte interface.[9] Despite that, the construction of an alloying electrode often results in uneven surfaces with high specific area because of the uncontrollable rate of the magnetron sputtering method, thus prompting the occurrences of hydrogen evolution reaction (HER) and corrosion.[10] On the contrary, building functional surface protective layer(s) is regarded as a more direct and efficient strategy for enhancing zinc anodes via redistributing the electric field, lowering nucleation, and promoting three-dimensional (3D) diffusion.[11] Till now, various coating layers have been explored, including metal layers,[12] polymers,[13] inorganic nanomaterials,[14] and two-dimensional (2D) materials,[15] which have shown elevated capability in inhibiting dendrite growth. Among all, metal layer coatings are particularly noteworthy for their high zinc affinity and exceptional anticorrosion properties, facilitating zinc nucleation and high CE. However, the synthesis of metal-coated zinc through in situ metallic displacement presents a challenge in controlling surface morphology, resulting in a high contact area and potentially triggering side reactions at the interface. In addition, while inorganic materials possess the features of being chemically inert to electrolytes, good mechanical properties to accommodate volume change, and good wettability to reverse electrolytes, it is challenging to realize atomic-level thin film via atomic layer deposition.[16] The functionalized polymer with polar groups can redistribute and guide the deposition behavior of Zn^{2+} but the inferior electric conductivity can probably cause sluggish Zn^{2+} diffusion. 2D materials such as graphene and MXene are more likely to induce the preferred (002) deposition of Zn owing to the compatible crystalline planes. Unfortunately, realizing high Zn^{2+} deposition capacity in symmetric cells is susceptible to short circuit during continuous plating.

A critical, yet often overlooked, aspect in the research of ZIBs is the preferential deposition of Zn^{2+} on the surfaces of interfacial coating layers rather than on

metallic zinc owing to its strong absorption capability, restricting the top-down transfer of Zn^{2+}. Consequently, the Zn anode fails to achieve high-capacity deposition and, even worse, potentially accelerates the onset of battery failure. Interestingly, the introduction of porous materials can induce a selective ion-sieving effect due to intricate electrolyte diffusion pathways. This unique property not only efficiently regulates the concentration field distribution and blocks undesirable species, such as H_2O molecule or SO_4^{2-} anion, but also facilitates the diffusion of Zn^{2+} along confined pathways and prevents stacking of deposited Zn layer.[17] Thus, such modification enables the zinc anode to attain higher areal capacities through a bottom-up deposition process, initiating from the metallic zinc surface and progressing upward toward the interfacial layer.

MXene ($Ti_3C_2T_x$) sheets with exceptional electric conductivity, hydrophilicity, and zincophilicity have been extensively employed in the metal anodes of ZIBs.[18–22] Regardless, the high plating areal capacity is often constrained by the limited downward transfer of Zn^{2+} beneath the interfacial coating layer. Herein, a kind of porous MXene flake (MXF), derived from facile alkaline etching of large lateral size MXene sheet (MXS) in water solution, is proposed as an interfacial layer to stabilize Zn electrodes when using carboxymethyl cellulose (CMC) as a binder. The MXF layer can not only guide uniform ion concentration and reduce nucleation overpotential but also shield the Zn electrode from contact with H_2O and SO_4^{2-}. Furthermore, the porous MXF layer allows the deep Zn^{2+} diffusion and deposition, generating a dense deposition layer in great comparison with MXS-coated anode (Zn@MXS), which is illustrated by density function theory (DFT) and characterization techniques, including scanning electron microscopy (SEM) and 3D laser scanning microscopy (LSM). Additionally, the quantum-sized MXene dots, resulting from the etching process, also play a crucial role in guiding the deposition behavior of Zn^{2+}. Consequently, the MXF-modified anode (Zn@MXF) delivers ultrastable Zn||Zn cell cycling over 2700 h at 1.0 mA cm^{-2} (1.0 mAh cm^{-2}) and satisfying CE of Zn||Cu cell at 2.0 mA cm^{-2} (0.5 mAh cm^{-2}). When assembled in full cells with α-MnO$_2$, the batteries harvest an elevated long-life cycling performance (191 mAh g^{-1} at 2.0 A g^{-1} after 2000 cycles) and remarkable rate capability (returning to 0.2 A g^{-1} without capacity decline).

2 | RESULTS AND DISCUSSION

Inspired by the ion-sieving effect, MXFs derived from few-layered MXene ($Ti_3C_2T_x$) sheets were constructed as an artificial solid electrolyte interphase layer for

reversible Zn plating/stripping. The Zn^{2+} deposition behavior of bare Zn and Zn@MXF anodes is illustrated in Figure 1A,B. As it is widely accepted that the notorious dendrite growth is lethal to battery cycling life, guiding uniform deposition of Zn^{2+} is particularly important, which is ascribed to uneven concentration field, high nucleation overpotential, and overexposure to electrolyte. First, the ionic distribution is effectively regulated by the coated MXF layer where the Zn^{2+} is preferentially absorbed by abundant surface-terminated groups (-OH, -O) after alkalic treatment, lowering the nucleation barrier owing to strong adsorption. Furthermore, the MXF layer majorly allows the permeation of Zn^{2+} instead of free water and anions that are repelled by electrostatic force, which vastly reduces the side reactions. On the contrary, the overexposed zinc metallic surface prompts various electrolyte components to react and compete with zinc ions, resulting in vigorous growth of dendrite and the formation of by-products. As verified by COMSOL Multiphysics, Figure 1C displays a strong localized concentration field from the bare electrode, which primarily triggers the continual deposition of protrudes. As deposition continues, the small protrudes evolve into large flakes of dendrites posing the risk of penetrating the separator (Figure S1). After introducing MXF layers, the localized concentration field is effectively homogenized along with the local current density (Figure 1D), beneficial from abundant functional groups providing nucleation sites. The differences in deeper deposition behavior between MXF and MXS coating
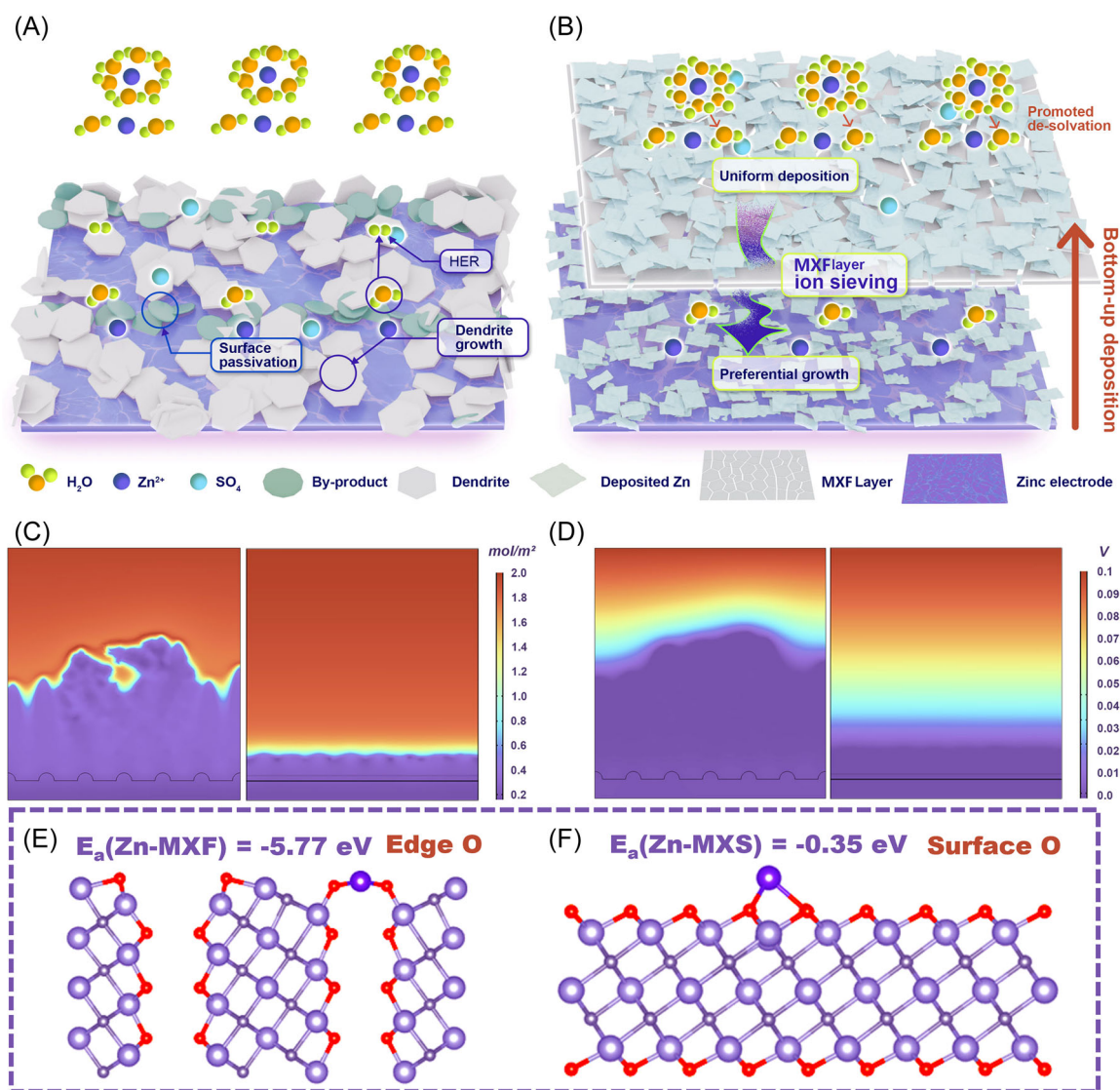

FIGURE 1 Schematic illustration of (A) bare Zn and (B) Zn@MXF impacting Zn^{2+} deposition behavior, respectively. (C) The concentration field distribution and (D) the electric field distribution of bare Zn (left) and Zn@MXF (right). Adsorption model of (E) MXS layer and (F) MXF layer on Zn^{2+} and corresponding adsorption energy.

layers were also studied by DFT calculations. The adsorption energy is vital to Zn^{2+} behavior and would affect the deposition underneath or above the coating layer. Figure 1E,F represents the structural model of MXF and MXS, respectively, showing that the thick and large lateral MXS were broken down into MXF, generating substantial defect sites for Zn^{2+} transport and nucleation. Distinctly, the calculated adsorption energy of Zn^{2+} on MXF (−5.77 eV) is markedly higher than that of MXS (−0.35 eV), indicating that the stronger binding ability is likely ascribed to the exposed edged O-terminated groups formed by OH^- etching. Consequently, the Zn^{2+} tends to traverse the MXF layer and preferentially deposit on the Zn electrode, generating gradient plating with high areal capacity.

The ion-sieving MXFs were prepared by a facile solution reaction via OH^- etching the few-layered MXS followed by freeze-drying. From SEM images (Figure S2), the MXS demonstrates large and thick lateral size owing to the restacking of MXS, which only allows the deposition to occur on the surface of the coating layer. After the etching treatment, the large size of MXS was exfoliated and cracked into MXF, resulting in a great number of exposed terminated groups (Figure S3). The characteristic bands of as-prepared samples were determined by Raman spectroscopy, as shown in Figure 2A. The peaks at 200, 400, and 600 are observed in MXF and MXS, showing that the main crystal structure of MXF is well reserved.[23] The X-ray diffraction (XRD) patterns are presented to identify the phase changes of the samples (Figure 2B). Notably, the typical (002) peak is seen in MXF and shifts to a lower 2θ value, indicating that the alkaline treatment is effective in exfoliating and etching the MXF. The peak located at
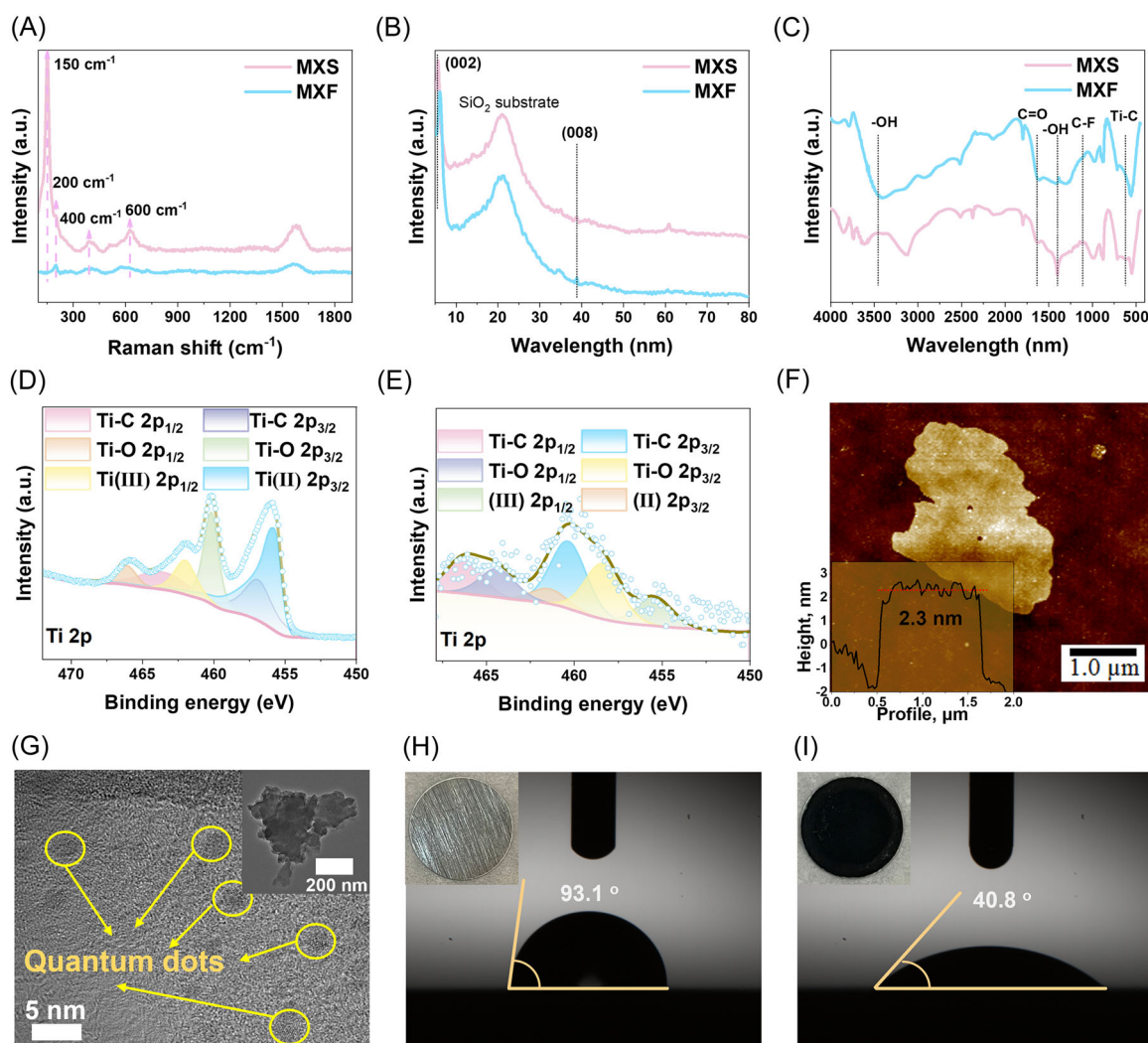

FIGURE 2 Characterization of as-prepared materials. (A) Raman spectra, (B) XRD patterns, and (C) FTIR spectra of MXS and MXF coating layers. Deconvoluted XPS high-resolution of Ti 2p: (D) MXS and (E) MXF. (F) AFM and (G) TEM images of MXF layer. Contact angles of (H) bare Zn and (I) Zn@MXF.

38.8° is indexed to the crystal plane of (008). The broad diffraction peak at around 22° is ascribed to the SiO_2 substrate during XRD scan.

Fourier-transformed infrared (FTIR) spectroscopy and X-ray photoelectron spectroscopy (XPS) were applied to analyze the surface bonding and valence state of the as-prepared samples. The FTIR spectrum (Figure 2C) shows that the MXS possesses distinct peaks at 1616, 1412, 1116.3, and 621.5 cm^{-1} corresponding to C=O, -OH, C–F, and Ti–O, respectively.[24] Furthermore, the disappearing C–F peak at 1116.3 and rising -OH peak at 3406 cm^{-1} in MXF suggest that the increase of the -OH terminated group is the result of the replacement of the F group under stirring in -OH containing solution. These results also show that the addition of -OH functional could provide more nucleation sites and an effectively uniform electric field. The XPS results reveal that MXS and MXF have matching characteristic bonds in each element (Figures 2D,E and S4). Especially, the Ti–C bond can be well deconvoluted in both spectrums from as-prepared samples, which again implies that the crystal structures after alkaline treatment are well maintained. The morphology of the MXF is further investigated using atomic force microscopy (AFM) and transmission electron microscopy (TEM). The AFM image shows the thickness of the MXF ranging from 1.84 to 2.75 nm with an average value of 2.3 nm (Figure 2F). The treated MXF exhibits obvious etching marks with rugged surfaces as shown in Figure S5A,B and the inset of Figure 2G. Surprisingly, the etching process can generate MXene quantum dots exfoliated from the MXene surface as we can see from Figures 2G and S5C, which not only increase absorption sites but also lower the nucleation barrier for Zn^{2+} as reported by many related works of quantum dots on modifying zinc anodes.[25–30] The incorporation of ion-sieving MXF and MXene quantum dots could dramatically improve the cycling life of Zn||Zn batteries by promoting Zn^{2+} transfer and thus inhibiting notorious dendrite growth.

The modified zinc electrodes were prepared by mixing coating materials such as MXF with sodium CMC binder and directly pasting the slurry onto zinc metal. The surface morphologies of the Zn@MXS electrode are displayed in Figure S6A,B, and it shows that the largely stacked layer-by-layer MXS forms the thick coating layer fully covering the zinc metal. In contrast, the MXF is composed of microparticles with considerable free space, which is beneficial to electrolyte permeation (Figure S7A,B). The thicknesses of the coating layer are both less than 10 μm as estimated from Figures S6C and S7C. The height profiles are also presented in Figures S6D and S7D, showing that the MXF has a more uniform surface. The wettability of the MXF layer demonstrates a lower contact angle than that of the MXF and bare electrode, which is inconsistent with the results in Figures 2H,I and S6E.

The symmetric Zn||Zn cells coupled with the MXF coating layer were carried out to prove their ability of elevating electrochemical performances. First, the rate performance of assembled cells is presented in Figure 3A, and the cells were cycled at 1.0 mA cm^{-2} for 40 h to stabilize the electrolyte/electrode interface. The Zn@MXF electrode exhibits stable polarization potential with 28, 33, 39, 48, 89, and 119 mV (Figure S8) at different current densities starting from 0.2 to 10.0 mA cm^{-2}. More impressively, when the current density was switched back to 2.0 mA cm^{-2}, it still maintained reversible plating/stripping for over 160 h. By contrast, the bare electrode only sustained the stabilization process and then went through a short circuit rapidly after cycling at 0.5 mA cm^{-2}. The rate performance of the CMC-coating Zn electrode was also tested, as shown in Figure S9A, to demonstrate the synergistic effect brought by the CMC binder. The Zn||Zn cell could also withstand stable cycling throughout the rate test except with fluctuating the curve at a high current density such as 2.0 mA cm^{-2}, which is probably associated with the dissolution of the CMC binder in the electrolyte. The long-life cycling performance test of symmetric cells was performed to evaluate the durability of the coating materials. As depicted in Figure 3B, the cells were tested at a current density of 1.0 mA cm^{-2}, and the effect on inhibiting dendrite growth is obvious. In detail, a larger polarization voltage is observed in the bare Zn||Zn cell, which only sustained 80 h during the repeated plating/stripping process. For the Zn@MXF electrode, it is evident that the cycling performance of symmetric cells was tremendously boosted up to 2700 h with gradually decreasing polarization voltage. When the current density was increased to 2.0 mA cm^{-2}, the cycling retention of Zn@MXF could also be greatly improved up to 2000 h in vivid contrast with bare zinc only lasting 25 h due to internal short circuit (Figure 3C).

The deposition kinetics can be explained by electrochemical impedance spectroscopy (EIS) of symmetric cells with or without the MXF coating layer before cycling. As shown in Figure 3D, both curves reflect the semicircle at high and medium frequencies corresponding to charge transfer impedance (R_{ct}). The interfacial electric conductivity of Zn@MXF is slightly higher than that of bare Zn owing to the lower conductivity of the MXF layer. The decreased R_{ct} value after MXF coating shows exceptional charge transfer capability, which is beneficial from the abundant surface functional groups on MXF providing sufficient contact between the electrolyte and electrode. In addition, chronoamperometry (CA) was carried out under
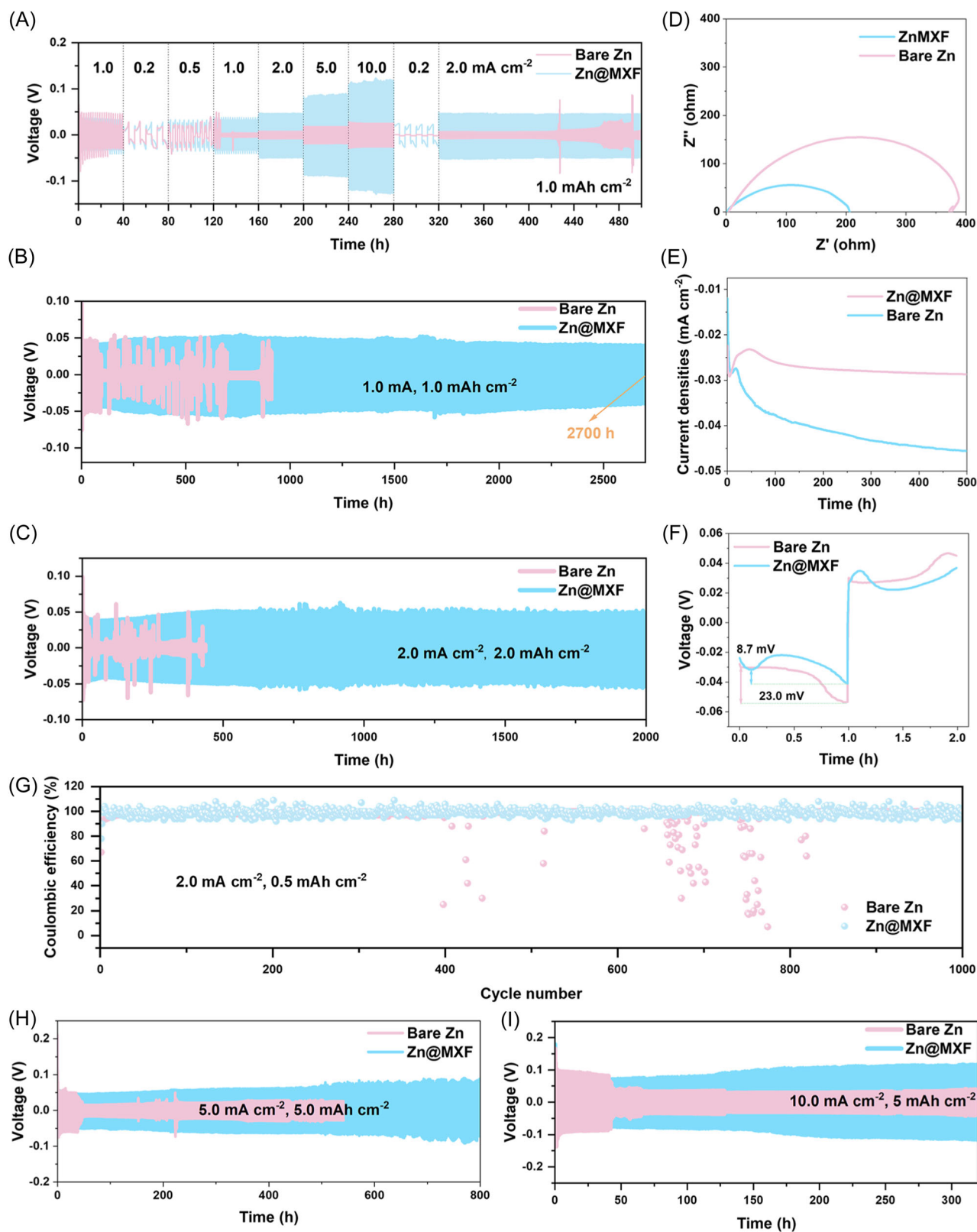
FIGURE 3 Stripping/plating of bare Zn and Zn@MXF. (A) Rate performance of symmetric cells at various current densities. Cycling performances of symmetric cells at (B) 1.0 mA cm^{-2} and (C) 2.0 mA cm^{-2}. (D) EIS of symmetric cells. (E) Chronoamperogram tested at an overpotential of -150 mV for 500 s. (F) Voltage–time profile of symmetric cells at 1.0 mA cm^{-2}. (G) CE test at 2.0 mA cm^{-2} (0.5 mAh m^{-2}). Cycling performances at a high current density of (H) 5.0 mA cm^{-2} and (I) 10.0 mA cm^{-2}.

an overpotential of -150 mV to analyze the Zn^{2+} diffusion behavior. As shown in Figure 3E, the bare electrode exhibits higher current response and an obvious increasing tendency within 150 s, suggesting that Zn^{2+} mainly diffuses in 2D mode resulting in continuous accumulation of Zn nuclei. In contrast, profiting from the uniform electric field and strong adsorption energy of MXF, a relatively steady 3D diffusion with smaller overpotential can be observed after slight current fluctuation within 50 s, which is favorable to forming plentiful nucleation sites. The lower nucleation overpotential could be achieved in the Zn@MXF electrode with only 8.7 mV in great contrast to the bare Zn electrode with 23.0 mV, and it also has an advantage over many reported works (Figure S10), indicating the lower nucleation barrier because of the stronger Zn affinity of MXF (Figure 3F). The above analysis suggests that the MXF-coated Zn anode could facilitate diffusion, homogenize the concentration field, and lower the nucleation barrier, effectively inhibiting the continuous growth of dendrites. The reversibility during the stripping/plating process of Zn anode is pivotal to the long cycling life of the batteries, and therefore, the CE of Zn||Ti cells was examined. Predictably, the Zn@MXF achieved a higher cycling life of 1000 cycles with an average CE of 99.2% at 2.0 mA cm^{-2} of 0.5 mAh cm^{-2}, which is a big enhancement as compared to bare Zn (Figure 3G). There is a climbing tendency of CE for Zn@MXF in the first few cycles, which is associated with the interfacial wetting process of the coating layer.[31] When the areal capacity was increased to 1.0 mAh cm^{-2}, the Zn@MXF||Ti asymmetric cells could stabilize within 200 cycles (Figure S11). As a result, the modified electrode could demonstrate outstanding rate capability and long cycling performance in symmetric cells with improved reaction Zn^{2+} kinetics.

The current density was further increased to the higher current densities of 5.0 and 10.0 mA cm^{-2} as presented in Figure 3H and Figure 3I, respectively. The polarization potential augmented distinctly for bare electrodes, and the cells quickly failed within 50 h of plating and stripping. Conversely, the MXF-coated zinc anode obtained a satisfying cycling life of 800 h at 5.0 mA cm^{-2} and over 300 h when the current density was raised to 10.0 mA cm^{-2}, showing the efficiency of lowering the nucleation barrier and uniformly distributing concentration field. The cycling results of the CMC binder were also tested as displayed in Figure S9B,C. Although the polarization voltage was reduced as compared to the bare electrode owing to a great number of polar carboxyl groups on CMC chains, the subsequent dissolution of CMC gradually exposed the metal zinc and finally resulted in notorious dendrite growth. The electrochemical performances of symmetric cells for MXS zinc anode (Zn@MXS) were also tested to display

the advantages of the Zn@MXF electrode. Given the functional terminated surface, the Zn@MXS can certainly distribute homogeneous electric fields, promote 3D diffusion, and reduce the nucleation barrier, which contributes to uniform deposition. As shown in Figure S12, Zn@MXS||Zn@MXS cells could sustain impressive stripping/stripping cycling life over 2000 h, a considerable improvement compared to bare Zn electrodes. However, when compared with the Zn@MXF electrode, the Zn@MXS electrode without ion-sieving effect could only withstand cycling life of 333, 329 h, and 96 h under higher current densities of 2.0, 5.0, and 10.0 mA cm^{-2}, respectively (Figure S13). The inferior results show that the deposition for the Zn@MXS electrode largely occurs on the surface of the MXS coating layer, rather than on the metallic zinc surface. The ion-sieving MXF coating allows Zn^{2+} to diffuse downward onto and then nucleate on the surface of the zinc anode, which is driven by the differences in electronic conductivity between the metallic zinc and the MXF layer. Voltage–time profiles of the bare Zn and Zn@MXF were performed at open-circuit voltages at a constant current of 5 mA. As shown in Figure S14, the calculated electronic conductivity for bare Zn is 27.62 mS cm^{-1} and for the MXF layer is 0.36 mS cm^{-1}. Therefore, the Zn^{2+} will preferentially deposit on metallic Zn rather than the inferior conductive MXF layer, which generates bottom-up deposition behavior with high plating capacity. Furthermore, the transference number of bare zinc and Zn@MXF was also calculated from Figure S15 using EIS and the current polarization method. Compared with a bare zinc electrode with a transference number of 0.73, Zn@MXF exhibits a remarkable value of 0.96, indicating that the faster transport of Zn^{2+} on MXF reduces polarization potential and forms a uniform concentration field. Consequently, the high transference number and poor electronic conductivity of the MXF coating layer are conducive to dendrite-free bottom-up deposition, which is superior to recently reported coating layers at various current densities (Figure S16 and Table S1).

The superficial changes of the electrodes in real time during Zn deposition were captured using in situ optical microscopy. As presented in Figure 4A, an irregular surface with some small protrusions was observed after 5 min deposition in the bare electrode at 5.0 mA cm^{-2}, and then these protrusions grew larger to form a dendrite cluster in the following deposition. By contrast, the Zn@MXF electrode presents a relatively smooth and compacted structure throughout the deposition process without dendrite and bubble formation (Figure 4B), which is attributed to the MXF modulating electric field distribution and blocking excessive free water. To further verify the positive effect on inhibiting dendrite
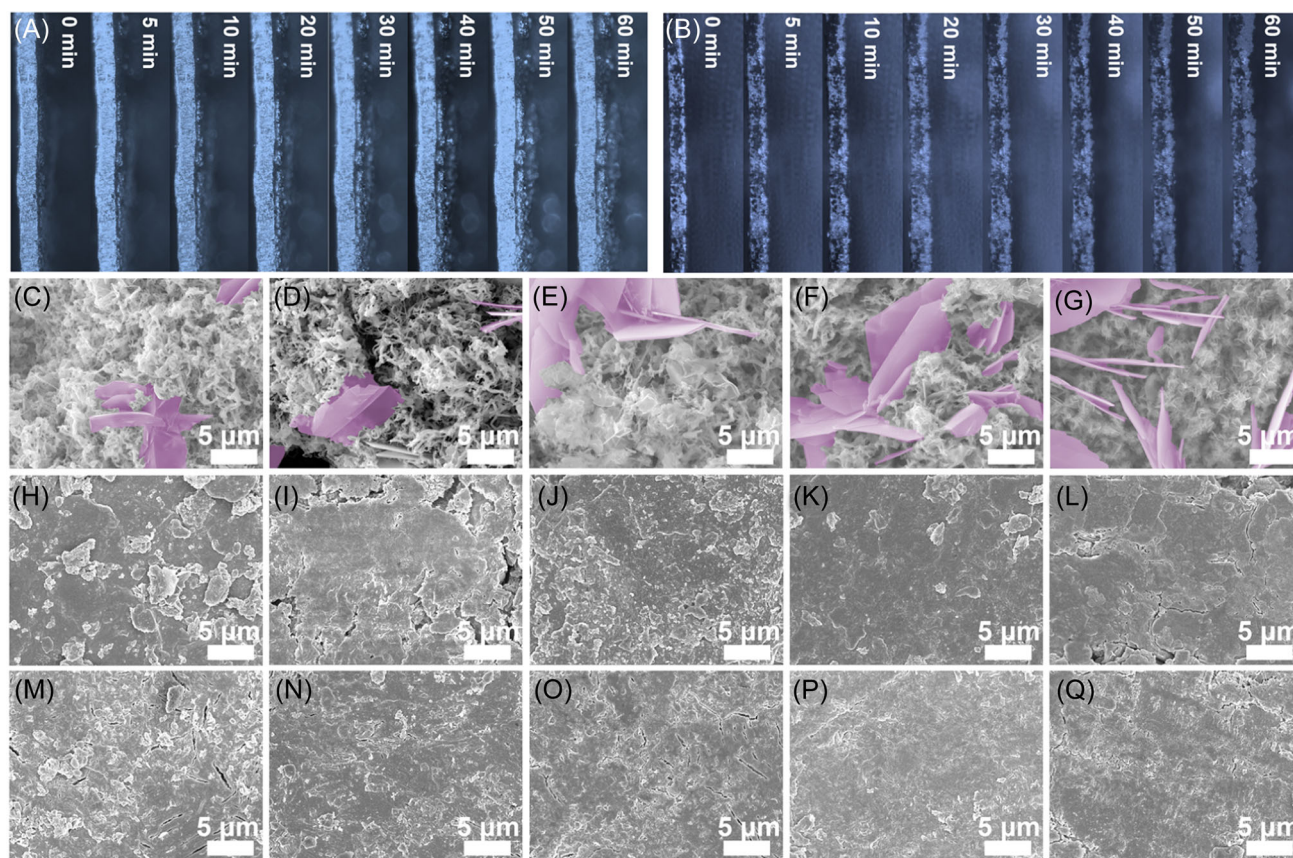
FIGURE 4 Optical observation during Zn^{2+} plating. In situ microscopic photos of (A) bare Zn and (B) Zn@MXF. SEM images of (C–G) bare Zn, (H–L) Zn@MXF, and (M–Q) Zn electrodes after peeling off the MXF coating layer at different plating times of 0.5, 1.0, 2.0, 5.0, and 10.0 h, respectively.

growth, the morphological evolution of bare zinc and Zn@MXF electrodes was evaluated via galvanostatic cycling at different current densities and areal capacities. Figure 4C–G compares the SEM images of bare zinc electrodes after plating for 0.5, 1.0, 2.0, 5.0, and 10.0 h with the current density of $1.0\,mA\,cm^{-2}$. Distinctly, small dendrites could be observed at small plating times of 0.5 and 1.0 h with filiform features, and then, these protuberances grew into larger and thicker flakes of dendrites after subsequent Zn deposition due to the "tip effect." Meanwhile, the by-products (ZHS) marked in purple formed notoriously along with increasing plating time, which is attributable to the direct contact between the electrolyte and zinc anode. By contrast, there is no existence of dendrites or by-product particles in Zn@MXF electrodes after plating at 0.5 and 1.0 h and even longer 10 h, indicating the uniform deposition induced by the MXF ion-sieving layer (Figure 4H–L). Furthermore, the above coating layers were peeled off from electrodes and further characterized to prove the bottom-up deposition. As displayed in Figure 4M–Q, the zinc anodes still manifest a uniform and flat deposition surface, and the small cracks on the zinc were produced

by the deposition of Zn^{2+}. The striking differences between the bare zinc electrode and MXF-coated electrode in deposition morphology imply that the functional MXF with abundant terminated groups and strong binding ability enables dendrite-free electrodes by forming a homogeneous electric field, providing plentiful nucleation sites and suppressing the side reactions.

The interfacial side reactions are also important to reversible long cycling in addition to inhibiting dendrite growth. The cyclic voltammetry (CV) of half cells was implemented to examine the Zn^{2+} plating/stripping behavior. As seen from Figure S17A,B, the CV curves of bare and Zn@MXF electrodes exhibit similar reduction/oxidation peaks corresponding to Zn^{2+} plating and Zn^0 stripping, revealing that the MXF ion-sieving layer has a merely negative impact on Zn^{2+} deposition behavior. Moreover, the overlapping curves show that the Zn@MXF has a larger CV area, which is the result of faster Zn^{2+} reaction kinetics and lower nucleation potential (Figure S17C). The Tafel curves were tested to monitor the corrosion rate of the electrodes under a three-electrode system. As presented in Figure 5A,
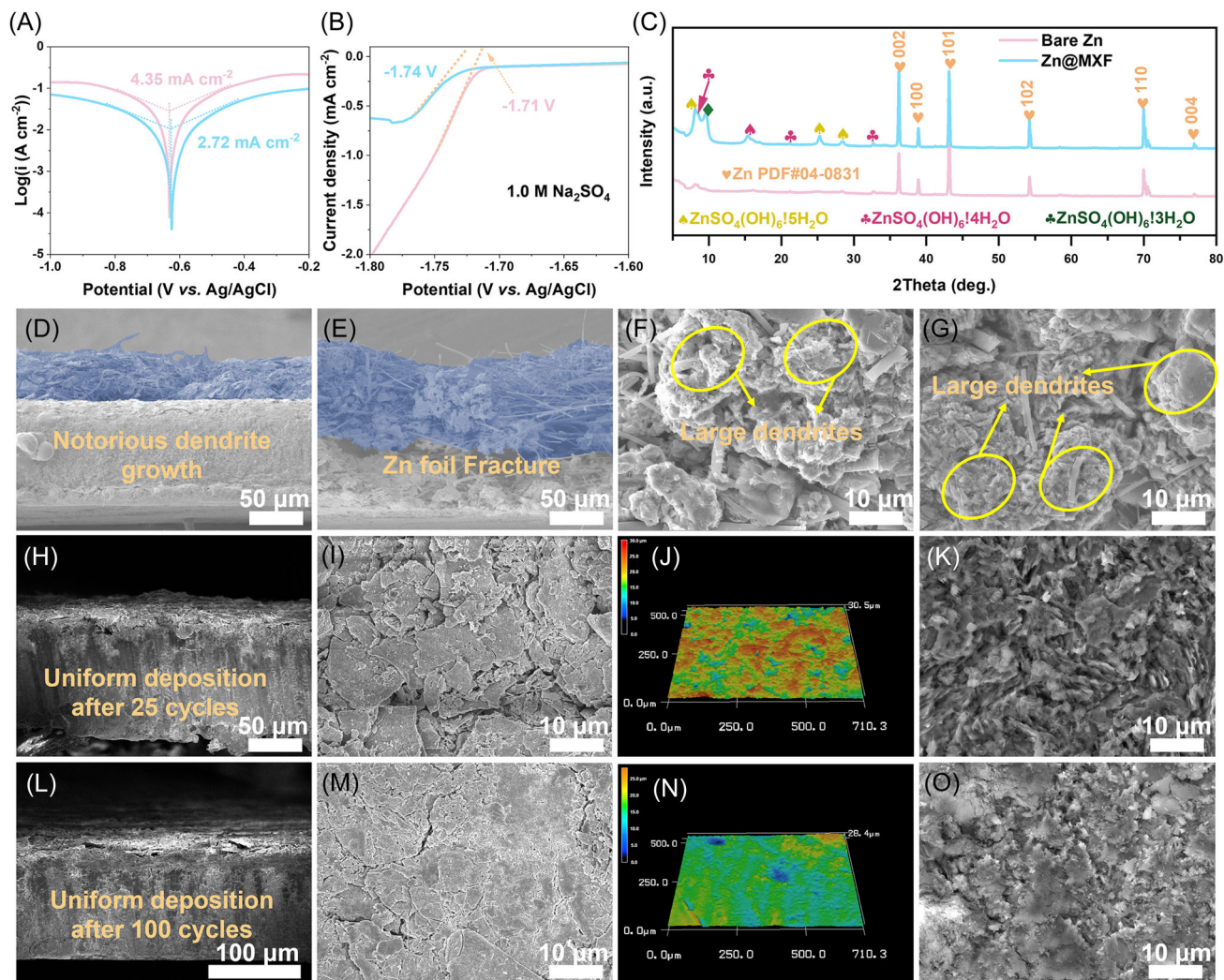
FIGURE 5 Anticorrosion and HER abilities. (A) Tafel curves of zinc electrodes under the three-electrode system. (B) Linear hydrogen evolution polarization in 1.0 M saturated Na_2SO_4. (C) XRD patterns of electrodes after soaked in $ZnSO_4$ for 14 days. SEM images in symmetric cells after different cycling at 2.0 mA cm^{-2} after 25 and 100 cycles, respectively: cross-sectional images of (D, E) bare Zn and (H, L) Zn@MXF. Top-view images of (F, G) bare Zn, (I, M) Zn@MXF, and (K, O) Zn electrodes after peeling off MXF layer. (J, N) Corresponding 3D optical photo of Zn@MXF.

a lower corrosion current density of 2.72 mA cm^{-2} was obtained by the Zn@MXF electrode while the bare electrode achieved a higher current density of 4.35 mA cm^{-2}. Contrastingly, a more positive self-corrosion potential could be observed in bare electrodes, indicating the exceptional anticorrosion capability of Zn@MXF. To study the effect on suppressing HER, linear sweep voltammetry was conducted in saturated 1.0 M Na_2SO_4 at a scan rate of 5.0 mV s^{-1}. The current response for Zn@MXF exhibits a slower decreasing tendency than that of bare electrodes, further confirming the function of suppressing side reactions (Figure 5B). The XRD patterns of bare and modified electrodes after soaked in $ZnSO_4$ electrolyte were recorded to prove the anti-corrosion effect (Figure 5C). Clearly, there are

obvious diffraction peaks in the bare electrode that can be indexed to multiple by-products of ZHS (Figure S18), which means that it could easily be induced to side reactions without protection. On the contrary, profited from the MXF layer with strong Zn^{2+} affinity and wettability, the diffraction peaks of ZHS could be hardly detected from the XRD patterns, which is consistent with SEM results (Figure S19). The above experimental results again unveil that the functional MXF layer can block excessive water and SO_4^{2-} to suppress the corrosion reaction and HER.

The morphological changes of electrodes after repeated stripping/plating at 2.0 mA cm^{-2} were measured using SEM characterization. When the symmetric cells cycled after 25 cycles, vigorously growing dendrites and by-products

emerged in the bare electrodeas shown in Figure S20A–C, due to the nonuniform electric field. The formation of small dendrite particles even aggravated after continuous stripping/plating of 100 cycles and finally produced uneven agglomerated morphology (Figure S20D–F). More directly, the cross-sectional images (Figure 5D) show irregular protrusions piling up vertically and intertwining with a great number of glass fibers, thereby causing a short circuit of cells. The uneven stripping even worsens after extended cycling for 100 cycles, and a large damage area can be observed from cross-sectional images (Figure 5E). In sharp contrast, the morphology of Zn@MXF after 25 cycles expectedly demonstrates a dendrite-free surface without accumulated dendrites penetrating the separator (Figures S21A–C and 5I), and surprisingly, the uniform deposition could sustain up to 100 cycles (Figures S22A–C and 5M), which can also be verified by the optical surface-profilometry images shown in Figure 5J,N. The cross-sectional images show a uniform, thin, and compact deposition layer, and the thicknesses of deposited zinc remain unchanged, indicating that the MXF functional layer is capable of buffering volume change of the anode (Figure 5H,L). For a better understanding of the MXF protective effect, the surface morphology of electrodes after peeling off the MXF layer is displayed in Figures S21D–F and 5K. As expected, the zinc anodes show a similar dendrite-free surface, firmly proving the ion-sieving effect and uniform distribution of the electric field. The uniform deposition is more obvious in the peeled electrode after 100 cycles (Figures S22D–F and 5O). In summary, the MXF layer with abundant functional groups and high specific area could not only effectively inhibit dendrite growth via bottom-up deposition but also reduce side reactions, such as corrosion and HER, thus enhancing the plating/stripping cycling lifespan.

To emphasize the function of the ion-sieving effect, we further examined the capability of plating high capacity of active Zn^{2+}. The application of ZIBs is more practical under small working current density to alleviate serious issues, for example, dendrite growth, as stressed by many works.[32–34] All anodic electrodes carried out the stripping/plating process at the small current density of $1.0\,mA\,cm^{-2}$ with increasing areal capacity. Figure 6A shows the cycling performances of symmetric cells after plating for 10 h with a depth of discharge (DOD) of 15%. The results are obvious that the bare Zn shortly suffered battery failure, and the Zn@MXS electrode only sustained 150 h before internal short circuit caused by continuous deposition. Conversely, the Zn@MXF achieved an inspiring cycling lifespan of over 1300 h, which is induced by the effective ion-sieving effect. As the plating times were increased to 20, 30, and 40 h, although the Zn@MXS exhibits enhanced performances

than bare Zn, the stability of plating/stripping is incomparable with Zn@MXF, which maintained 600, 300, and 280 h of cycling with DOD of 30%, 45%, 60%, respectively, as shown in Figures S23 and 6B. Furthermore, the morphologies of the electrodes after cycling were also characterized to display uniform deposition. The existence of dendrite nanoflakes can be seen from the MXS electrode after 10 h of plating, implying the inefficiency of regulating the electric field (Figure 6C). Subsequently, micro and large flakes of dendrites started to form, as illustrated in yellow, with increasing plating times of 20 and 30 h (Figure 6D,E). When the cells cycled for 40 h were disassembled, a great deal of disordered glass fibers penetrated by larger dendrite particles were observed, signifying the short circuit of the cells (Figure 6F). Distinctly, the smooth morphologies of the Zn@MXF electrodes are unveiled in Figure 6G–J throughout the plating process, demonstrating the impressive ability to homogenize the electric field, facilitate 2D diffusion, and reduce nucleation overpotential. The detailed working mechanism can be illustrated in Figure 6K,L. During the plating process, the Zn^{2+} transporting to the surface of the anode accumulates at the electrolyte/electrode interface, resulting in uneven distribution of the concentration field. Typically, the Zn^{2+} would deposit on the tip of protrusion on the bare electrodes, generating randomly distributing microshapes of dendrites, as depicted in Figures S24 and S25. Despite that the existence of pure MXS could effectively regulate the electric field owing to the high zincophilicity proved by charge difference density (Figure S26), the initial deposited Zn layer covering the surface of the coating layer would weaken the homogenizing effect during afterward deposition owing to Zn^{2+} losing direct contact with MXS. In consequence, a large dendrite would form, and Zn@MXS could obtain low plating capacity even under a small current density (Figure S27). Unlike the MXS layer, the functional MXF layer can effectively avoid the above issues when endowed with an ion-sieving effect, thereby inducing bottom-up deposition for high plating capacity. The optical photos all demonstrate more uniform morphologies under different current densities, as shown in Figure S28. The above experimental results firmly show that the ion-sieving MXF layer contributes to a dendrite-free anode with high plating capacity via facilitating 2D diffusion and promoting Zn^{2+} reaction kinetics.

The full-cell electrochemical performances were further tested to verify the practical feasibility of the Zn@MXF anode when paired with the α-MnO$_2$ cathode, which was synthesized using a typical hydrothermal method. The rate capability test presents a higher
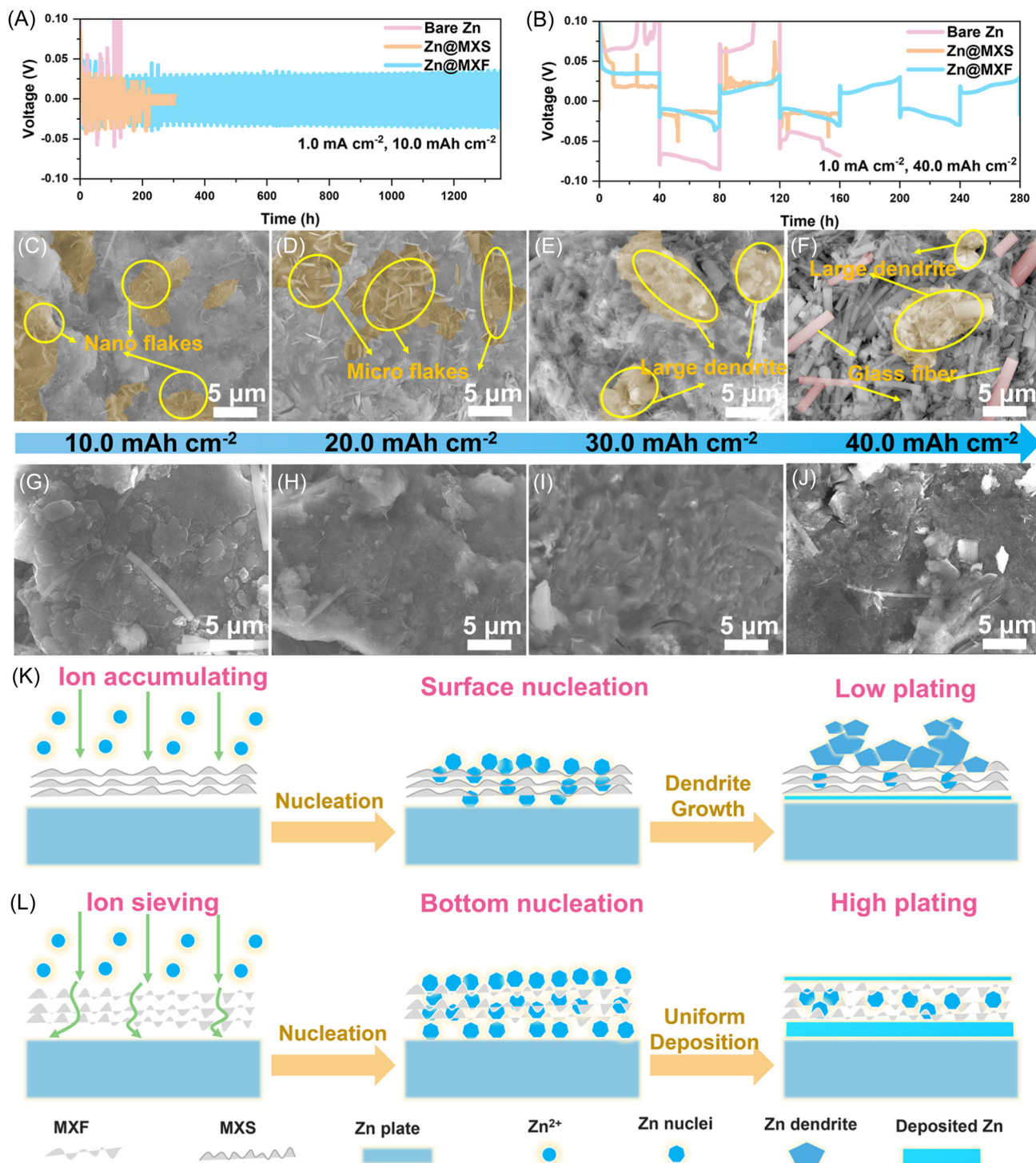
FIGURE 6 High plating capacity induced by ion-sieving effect. Cycling performance of symmetric cells at 1.0 mA cm^{-2} under plating for (A) 10 h and (B) 40 h. SEM images of Zn electrodes of (C–F) bare Zn and (G–J) Zn@MXF after plating for 10, 20, 30, and 40 h at 1.0 mA cm^{-2}, respectively. Schematically depicting the bottom-up deposition induced by (K) MXF layer via ion-sieving effect and (L) MXS layer via direct deposition.

discharge capacity of Zn@MXF than that of bare Zn, delivering 292, 270, 227, 158, and 112 mAh g^{-1} at the current density of 0.2, 0.5, 1.0, 2.0, and 3.0 Ag^{-1}, respectively (Figure 7A). When the current density

returned, the discharge-specific capacity could be recovered. The cycling life was compared at the current density of 0.5 Ag^{-1}, and the capacity retention was 74.7% with 168 mAh g^{-1} after 500 cycles for Zn@MXF, as
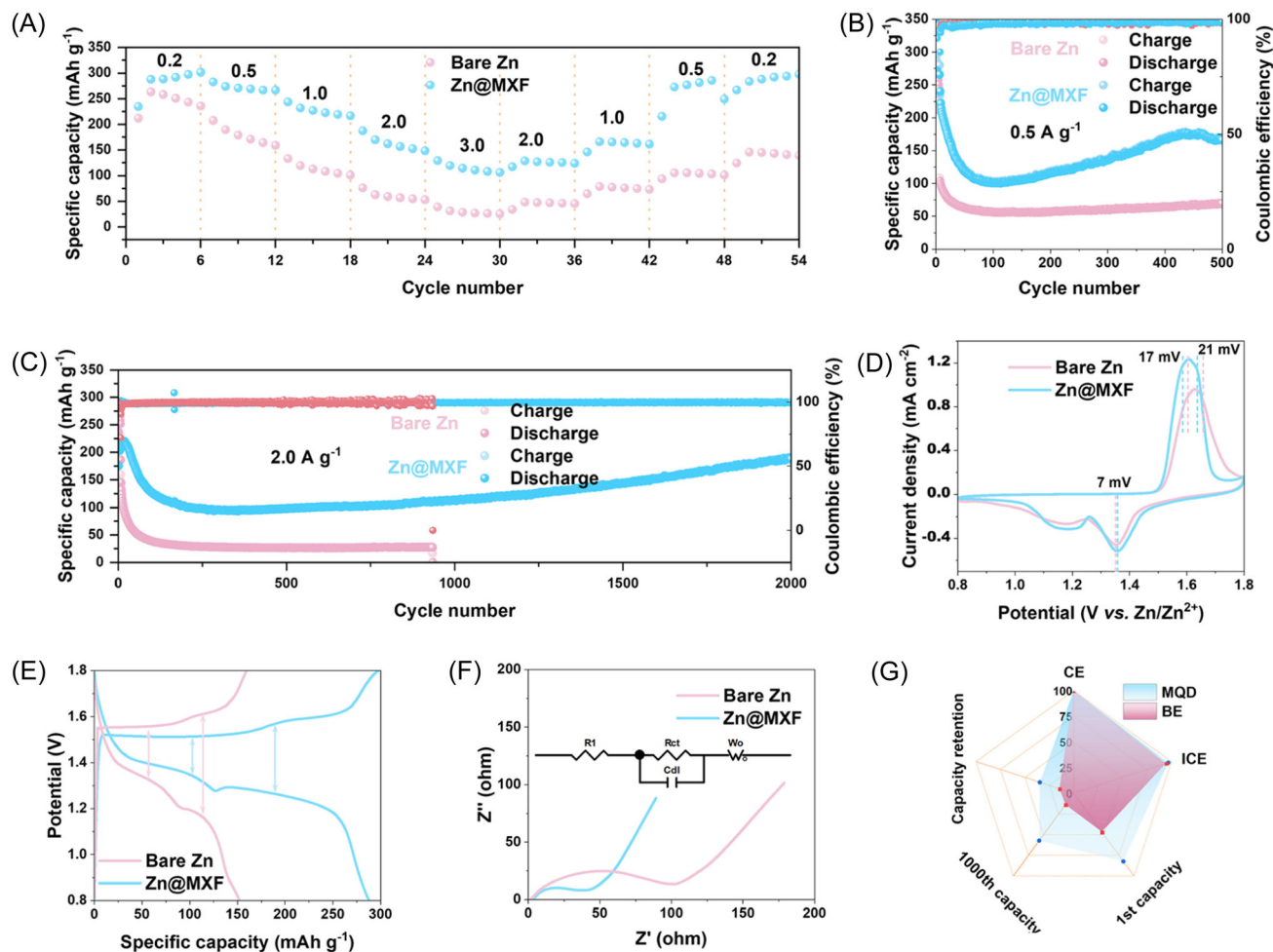
FIGURE 7 Evaluation of electrochemical performances in full cells. (A) Rate capability of bare Zn and Zn@MXF at different current densities. Long-term cycling performances at (B) 0.5 A g^{-1} and (C) 2.0 A g^{-1}. (D) CV curves. (E) Voltage-capacity curve plotted from rate test at 0.2 A g^{-1}. (F) EIS result and (G) radar chart for evaluation of cycling performance at 2.0 A g^{-1}.

compared to that of bare Zn of 65.0% with 71 mAh g^{-1} (Figure 7B). Even cycled at 2.0 A g^{-1}, the bare Zn was susceptible to short circuits while Zn@MXF maintained 190 mAh g^{-1} after 2000 cycles with 86% capacity retention (Figure 7C). The stable cycling reversibility can be revealed by CV curves, where the Zn@MXF anode attained a lower hysteresis voltage than the bare Zn anode (Figure 7D). Furthermore, the galvanotactic charge/discharge curves for Zn@MXF with smaller polarization voltage reflect the improved Zn^{2+} transport kinetics at the electrode/electrolyte interface (Figures 7E and S29), which is consistent with the EIS result (Figure 7F). Thus, the Zn@MXF could greatly surpass the bare Zn in full-cell performances at different current densities and cycling tests (Figure 7G). The large capacity improvement of Zn@MXF is attributed to the strong bonding ability, abundant nucleation sites, promoted 2D diffusion, and ion-sieving of the MXF functional coating layer.

3 | CONCLUSION

In summary, a functional MXF protective layer is designed via a facile low-cost doctor blade of MXF slurry using CMC as the binder to maximize the plating efficiency of Zn^{2+}. The deposition mechanism of Zn^{2+} induced by the functional MXF layer is unveiled by various characterization measurements, DFT, and finite element simulation. In detail, the polar groups (-OH) on the MXF protective layer have strong Zn affinity with Zn^{2+} and provide abundant zincophilic nucleation sites, effectively homogenizing the surface electric field, promoting 2D diffusion, and lowering the nucleation barrier. Furthermore, the process of fragmentating MXS into MXF dramatically boosts bottom-up deposition for high plating capacity owing to the ion-sieving effect. Meanwhile, the quantum-sized MXene dots produced from the etching process also play an important role in regulating Zn^{2+} deposition behavior. Consequently, the

sophisticatedly designed coating layer manifests a low nucleation potential (8.7 mV) and a long cycling lifespan in symmetric cells (2700 h, $1.0 \, \text{mA} \, \text{cm}^{-2}$) and half cells (99.2% at $2.0 \, \text{mA} \, \text{cm}^{-2}$). Even at the high plating capacity of $10–40 \, \text{mAh} \, \text{cm}^{-2}$, Zn@MXF exhibits exceptional cycling retention as compared to bare Zn and Zn@MXS. The MnO_2//Zn@MXF full cells achieve a high discharge specific capacity of $190 \, \text{mAh} \, \text{g}^{-1}$ at $2.0 \, \text{A} \, \text{g}^{-1}$ after 2000 cycles with 86% capacity retention. This work was inspired by the ion-sieving concept, which would blaze a path on constructing high plating capacity at a small current density for practical application.

CONFLICT OF INTEREST STATEMENT
The authors declare that there are no conflicts of interests.

ORCID
Bingang Xu http://orcid.org/0000-0002-1277-8747

REFERENCES
1. Liu Y, Xie B, Hu Q, et al. Regulating the helmholtz plane by trace polarity additive for long-life Zn ion batteries. *Energy Storage Mater*. 2024;66:103202.
2. Lu H, Hu J, Wei X, et al. A recyclable biomass electrolyte towards green zinc-ion batteries. *Nat Commun*. 2023;14(1):4435.
3. Lu H, Hu J, Zhang Y, et al. 3D Cold-Trap environment printing for long-cycle aqueous Zn-ion batteries. *Adv Mater*. 2023;35(9):2209886.
4. Xie B, Hu Q, Liao X, et al. Multifunctional electrolyte toward long-life zinc-ion batteries: synchronous regulation of solvation, cathode and anode interfaces. *Adv Funct Mater*. 2024;34(6):2311961.
5. Liu X, Cao Y, Wang H, et al. Phytic acid cross-linked and Hofmeister effect strengthened polyvinyl alcohol hydrogels for zinc ion storage. *Chem Commun*. 2024;60(5):554-557.
6. Wang T, Yao K, Li K, Yu JS. Influence of MXene-assisted multifunctional interface on zinc deposition toward highly reversible dendrite-free zinc anodes. *Energy Storage Mater*. 2023;62:102921.
7. Liu X, Xu B, Lu J, et al. A multifunctional zwitterion electrolyte additive for highly reversible zinc metal anode. *Small*. 2023;20(12):2307557.
8. Li C, Kingsbury R, Zhou L, Shyamsunder A, Persson KA, Nazar LF. Tuning the solvation structure in aqueous zinc batteries to maximize Zn-ion intercalation and optimize dendrite-free zinc plating. *ACS Energy Lett*. 2022;7(1):533-540.
9. Li B, Yang K, Ma J, et al. *Angew Chem*. 2022;134(47):202212587.
10. Li R, Du Y, Li Y, et al. Alloying strategy for high-performance zinc metal anodes. *ACS Energy Lett*. 2022;8(1):457-476.
11. Li C, Wang L, Zhang J, et al. Roadmap on the protective strategies of zinc anodes in aqueous electrolyte. *Energy Storage Mater*. 2022;44:104-135.
12. Hong L, Wang LY, Wang Y, et al. Toward hydrogen-free and dendrite-free aqueous zinc batteries: formation of zincophilic protective layer on Zn anodes. *Adv Sci*. 2022;9(6):2104866.
13. Wang Y, Guo T, Yin J, et al. Controlled deposition of zinc-metal anodes via selectively polarized ferroelectric polymers. *Adv Mater*. 2022;34(4):2106937.
14. Zhang S, Ye M, Zhang Y, Tang Y, Liu X, Li CC. Regulation of ionic distribution and desolvation activation energy enabled by in situ zinc phosphate protective layer toward highly reversible zinc metal anodes. *Adv Funct Mater*. 2023;33(22):2208230.
15. Fan C, Meng W, Li D, Jiang L. Stratified adsorption strategy facilitates highly stable dendrite free zinc metal anode. *Energy Storage Mater*. 2023;56:468-477.
16. He H, Qin H, Wu J, et al. Engineering interfacial layers to enable Zn metal anodes for aqueous zinc-ion batteries. *Energy Storage Mater*. 2021;43:317-336.
17. Gan H, Wu J, Zhang F, Li R, Liu H. Uniform Zn^{2+} distribution and deposition regulated by ultrathin hydroxyl-rich silica ion sieve in zinc metal anodes. *Energy Storage Mater*. 2023;55:264-271.
18. Chen Q, Wei Y, Zhang X, et al. Vertically aligned MXene nanosheet arrays for high-rate lithium metal anodes. *Adv Energy Mater*. 2022;12(18):2200072.
19. Wang Z, Huang Z, Wang H, et al. 3D-printed sodiophilic V_2CT_x/rGO-CNT MXene microgrid aerogel for stable Na metal anode with high areal capacity. *ACS Nano*. 2022;16(6):9105-9116.
20. Zhu X, Li X, Essandoh MLK, et al. Interface engineering with zincophilic MXene for regulated deposition of dendrite-free Zn metal anode. *Energy Storage Mater*. 2022;50:243-251.
21. An Y, Tian Y, Man Q, et al. Highly reversible Zn metal anodes enabled by freestanding, lightweight, and zincophilic MXene/nanoporous oxide heterostructure engineered separator for flexible Zn-MnO2 batteries. *ACS Nano*. 2022;16(4):6755-6770.
22. Park JM, Jana M, Baek SH, et al. MXene ink hosting zinc anode for high performance aqueous zinc metal batteries. *J Energy Chem*. 2023;76:187-194.
23. Naguib M, Kurtoglu M, Presser V, et al. Two-dimensional nanocrystals produced by exfoliation of Ti_3AlC_2. *Adv Mater*. 2011;23(37):4248-4253.
24. Xue Q, Zhang H, Zhu M, et al. Photoluminescent Ti_3C_2 MXene quantum dots for multicolor cellular imaging. *Adv Mater*. 2017;29(15):1604847.
25. Wang F, Lu H, Zhu H, et al. Mitigating the interfacial concentration gradient by negatively charged quantum dots toward dendrite-free Zn anodes. *Energy Storage Mater*. 2023;58:215-221.
26. Zhang H, Guo R, Li S, et al. Graphene quantum dots enable dendrite-free zinc ion battery. *Nano Energy*. 2022;92:106752.

27. Zhang J, Zhao Z, Yang Z, et al. A high-performance zinc anode enabled by carbon quantum dots with H$_2$O-structure-regulating capabilities. *Energy Storage Mater.* 2023;61:102904.

28. Zhang H, Li S, Xu L, et al. High-yield carbon dots interlayer for ultra-stable zinc batteries. *Adv Energy Mater.* 2022; 12(26):2200665.

29. Wang H, Zhou A, Hu X, et al. Bifunctional dynamic adaptive interphase reconfiguration for zinc deposition modulation and side reaction suppression in aqueous zinc ion batteries. *ACS Nano.* 2023;17(12):11946-11956.

30. Zhang W, Dong M, Jiang K, et al. Self-repairing interphase reconstructed in each cycle for highly reversible aqueous zinc batteries. *Nat Commun.* 2022;13(1):5348.

31. Hao J, Li B, Li X, et al. An in-depth study of Zn metal surface chemistry for advanced aqueous Zn-ion batteries. *Adv Mater.* 2020;32(34):2003021.

32. Tang B, Shan L, Liang S, Zhou J. Issues and opportunities facing aqueous zinc-ion batteries. *Energy Environ Sci.* 2019; 12(11):3288-3304.

33. Yang J, Yin B, Sun Y, et al. Zinc anode for mild aqueous zinc-ion batteries: challenges, strategies, and perspectives. *Nano-Micro Lett.* 2022;14(1):42.

34. Ji X, Nazar LF. Best practices for zinc metal batteries. *Nat Sustain.* 2024;7(2):98-99.

SUPPORTING INFORMATION

Additional supporting information can be found online in the Supporting Information section at the end of this article.

How to cite this article: Liu X, Xu B, Deng S, et al. Ion-sieving MXene flakes with quantum dots enable high plating capacity for dendrite-free Zn anodes. *Carbon Energy.* 2024;6:e603. doi:10.1002/cey2.603